Phase diagram up to 105 GPa and mechanical strength of HfO_2

Yahya Al-Khatatbeh,[1] Kanani K. M. Lee,[1,2] and Boris Kiefer[1]
[1]*Department of Physics, New Mexico State University, Las Cruces, New Mexico 88003-8001, USA*
[2]*Department of Geology and Geophysics, Yale University, New Haven, Connecticut 06511, USA*
(Received 27 July 2010; revised manuscript received 23 September 2010; published 13 October 2010)

Using high-resolution synchrotron powder x-ray diffraction, we have investigated the stability and equation of state (EOS) of hafnia HfO_2 phases under high pressures before and after laser heating to high temperatures. We observe three phases with increasing pressure: baddeleyite (monoclinic, MI), orthorhombic I (OI), and cotunnite (orthorhombic, OII). The OII phase is stable up to a pressure of at least 105 GPa before and after laser heating to ~1800 (±200) K. We provide experimental EOSs for the observed phases. The present results for MI-HfO_2 EOS are distinct from previous measurements yielding an ambient-pressure volume (V_0) of 34.50 (±0.04) Å^3/f.u. and an ambient-pressure bulk modulus K_0 of 185 (±23) GPa, assuming $K_0'=4$. In contrast, the experimental EOSs of OI and OII are in good agreement with previous studies. The measured EOSs are consistent with our density-functional theory calculations. The large volume decrease across the OI→OII phase transition as obtained from both our experiments and calculations is ~9%. Despite the large increase in density and high bulk modulus of OII-HfO_2, we find, using scaling relations, that all HfO_2 phases show similar mechanical hardness (H) of ~10–12 GPa, too low for HfO_2 to be considered a superhard material.

DOI: 10.1103/PhysRevB.82.144106 PACS number(s): 81.40.Vw, 31.15.A−, 64.70.K−, 61.50.Ks

I. INTRODUCTION

Due to its excellent structural stability and dielectric properties, hafnia is a material with a wide range of industrial applications in resistant coatings[1] and in electronic materials as gate insulators.[2] Furthermore, hafnia has received attention as an oxide material with potentially superhard high-pressure phases.[3–9] The mechanical hardness (H) of OII-HfO_2 has been measured for recovered samples and was found to be in the range of 6–13 GPa.[10] Therefore hafnia does not qualify as a superhard material ($H>40$ GPa) but the hardness measurements were thought to be biased by poor sintering conditions.[10] As a result, many experimental[4,5,9,11–18] and theoretical[3,6,8,19] studies have investigated the high-pressure/high-temperature behavior of HfO_2. However, previous experimental studies on the stability and equation of state (EOS) of the high-pressure OII phase are limited to pressures less than 71 GPa at room temperature[5,9,11,13,16–18] and below 25 GPa at elevated temperatures.[4,12,14–16]

Similar to transition-metal dioxide zirconia ZrO_2, the ambient temperature phase sequence is baddeleyite (MI, monoclinic, space group: $P2_1/c$) → orthorhombic I (OI, orthorhombic, space group: $Pbca$) → orthorhombic II (OII, orthorhombic, space group: $Pnma$).[5,16] The ambient pressure/high-temperature phases of HfO_2 are tetragonal (space group: $P4_2/nmc$) and cubic (fluorite, space group: $Fm3m$),[20,21] respectively. Other structures have also been reported for HfO_2 at high pressures; namely, tetragonal[9,13,17] and orthorhombic[13,17] phases, although these structures have not been reproduced since their identification.[9,17] Among these phases, the high-pressure OII phase has attracted great attention since it is dense and quenchable to ambient conditions with a high bulk modulus.[4,5,12,16] Thus, it has been speculated that this phase may be superhard.[3–8] The reported bulk modulus of MI-HfO_2 ranges from 145 (Ref. 17) to 284 GPa,[5] whereas bulk modulus-volume systematics give an intermediate value of ~200 GPa.[22] Thus, very large uncertainties exist in the measured EOS even for the ambient pressure phase of HfO_2. These large variations in the bulk modulus also suggest a different assessment is necessary if it is to be used as a proxy for mechanical hardness.[7,9,23]

In general, it is expected that a material becomes harder with decreasing volume, either within a single phase or across volume-reducing phase transitions.[24] Thus, if high-pressure phases can be recovered at ambient conditions, this may provide a promising route for the synthesis of materials with enhanced mechanical properties.[25,26] It has been suggested previously that a similar synthesis procedure could be applicable to HfO_2 (Refs. 3–9) and if successful, this would increase the pool of currently available superhard materials. On the one hand, if hardness is dominated by volumetric effects, then the bulk modulus is expected to be a suitable proxy for the mechanical strength of a material.[7,9,23] On the other hand, if shear displacement is dominant, then the shear modulus should be a better proxy for the mechanical strength of a material.[27,28]

As the OII-HfO_2 phase has been suggested to be much harder than the low-pressure phases,[3–8] OII has been investigated repeatedly over the past two decades, with a focus on the equation of state, phase stability, quenchability, elastic properties, and the thermal (meta)stability at ambient pressure.[4–6,8,12,16,19,29–31] On the other hand, much less attention has been paid to the EOSs of the low-pressure phases MI and OI,[4,5,17] and their elastic constants and related properties have not been measured or calculated previously.

In this study, we investigate the phase stability and equations of state of HfO_2 up to a pressure of ~105 GPa at ambient temperature before and after laser heating to ~1800 (±200) K. Furthermore, we augment our experiments with *first-principles* density-functional theory (DFT) calculations to test the stability and compressional behavior of our experimentally observed HfO_2 phases. We also estimate the hardness of these phases at ambient pressure directly from our computational results using a recently proposed scaling

TABLE I. Experimental conditions for HfO_2 sample runs. There are three unheated and three heated experiments at different pressures (20, 35, and 105 GPa) to ~1800 (±200) K. The stability range for the observed phases in each experiment is also given. For the heated experiments, all diffraction patterns were taken after cooling to room temperature.

Run	Heating history	Pressure medium	Phase stability range	Pressure-quenched phases
1	Not heated	Methanol-ethanol-water[a]	MI: up to ~14 GPa (compression) and from ~5 to 0 GPa (decompression) and OI: from ~9 to 19 GPa (compression) and from ~19 to 0 GPa (decompression)	MI and OI
2	Not heated	NaCl[b,c]	MI: up to ~11 GPa (compression), OI: from ~11 to 41 GPa (compression), and OII: from ~35 to 55 GPa (compression) and from ~55 to 0 GPa (decompression)	OII
3	Not heated	NaCl[b,c]	OII: from ~53 to 94 GPa (compression)	OII
4	Heated to ~1800 K at~20 GPa	NaCl[b,c]	OI: from ~20 to 27 GPa (compression, postheat) and OII: from ~20 to 37 GPa (compression, postheat) and from ~37 to 0 GPa (decompression, postheat)	OII
5	Heated to ~1800 K at ~35 GPa	NaCl[b,c]	OI: at ~36 GPa (compression, preheat), OII: at ~35 GPa (compression, postheat) and from ~35 to 0 GP (decompression, postheat), and MI: at 0 GPa (decompression, postheat)	MI and OII
6	Heated to ~1800 K at ~105 GPa	NaCl[b,c]	OII: from ~51 to 105 GPa (compression, preheat) and at ~105 (compression, postheat) and from ~105 to 0 GPa (decompression, postheat)	OII

[a]Reference 33.
[b]Reference 34.
[c]Reference 35.

model.[32] To better understand the correlations between hardness and bulk/shear moduli, we compute the elastic constants of each room-temperature HfO_2 phase and calculate the corresponding aggregate shear moduli.

II. EXPERIMENTAL METHODS

A polycrystalline sample of 99.95% HfO_2 baddeleyite powder (Alfa Aesar, grain size: <5 μm) was used as a starting material in our diamond-anvil cell (DAC) experiments. We performed six independent high-pressure DAC experiments to study the phase relations in HfO_2 (Table I). In five experiments, sodium chloride (NaCl) was used as a pressure-transmitting medium that provided quasihydrostatic conditions and acted as a pressure calibrant.[34,35] For one room-temperature experiment up to ~19 GPa, a mixture of methanol-ethanol-water (16:3:1 by volume) was used as a pressure-transmitting medium.[33] We also loaded 1–2 ruby spheres, <10 μm in diameter, into the DAC to obtain a second independent pressure measurement.[36] The pressures as inferred from the ruby and/or the NaCl calibrants generally agreed to within 4–11 % and pressure reported are averaged. The uncertainty in pressure was determined by averaging the measured pressures from NaCl and ruby. Rhenium (Re) gaskets of initial thicknesses of 220–280 μm were precompressed to thicknesses of 25–35 μm. The sample and pressure calibrants were placed in a 100 or 150 μm hole in the center of the gasket and compressed between a pair of matched 200 or 300 μm culet diamonds, respectively. In three of the experimental runs, the sample was laser heated at high pressures using an ~1 μm near-infrared laser[37] for ~10 min up to ~1800 (±200) K as determined by spectroradiometry.[38] Subsequently, the sample was temperature quenched and x-rayed at ambient temperature (Table I, Fig. 1, runs 4–6). While these experiments explore the T-quenched part of the high-T portion of the high-pressure phase diagram, we also collected angular-dispersive x-ray diffraction (XRD) at room temperature on cold compression and on decompression (Table I, Fig. 1, runs 1–3). XRD patterns were obtained using a MAR345 image plate at the HP-CAT beamline (λ=0.36802 or 0.36940 Å) at the Advanced Photon Source (APS) at Argonne National Laboratory, and at the B2 beamline (λ=0.49594 Å), Cornell High Energy Synchrotron Source (CHESS), Cornell University. For heated experiments, samples were laser heated at 20, 35, and 105 GPa. Laser heating was used to anneal the sample and minimize deviatoric stress as well as to add a modest amount of thermal energy to the system to facilitate otherwise kinetically hindered phase transitions. This is particularly important for materials such as hafnia where the increasing coordination number requires formation of new bonds. All XRD measurements, whether laser heated or not, were taken at

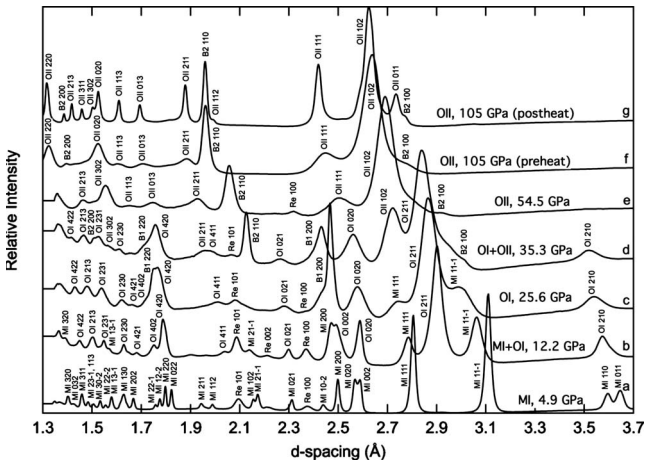

FIG. 1. XRD patterns at various pressures during compression of HfO_2 runs 1 and 2 (unheated) and run 6 (heated). Baddeleyite (MI), orthorhombic I (OI), orthorhombic II (OII), and NaCl (B1, B2) Miller indices are shown for respective XRD reflections. A rhenium reflection from the gasket is marked with Re. Patterns shown are taken at the following pressures: (a) 4.9 (± 0.1) GPa, (b) 12.2 (± 0.1) GPa, (c) 25.6 (± 0.3) GPa, (d) 35.3 (± 1.0) GPa, (e) 54.5 (± 0.1) GPa, (f) 105.2 (± 10.6) GPa (preheat), and (g) 105.3 (± 10.3) GPa (postheat).

room temperature. One-dimensional patterns were obtained from the two-dimensional patterns by using the FIT2D software.[39] Unit-cell volumes were determined using 6–15 reflections for MI, 5–14 reflections for OI, and 5–11 reflections for OII. A Birch-Murnaghan (BM) (Ref. 40) EOS was used to determine the compressional behavior of the observed HfO_2 phases. The third-order Birch-Murnaghan EOS is given by[40]

$$P = \frac{3}{2}K_0[(V/V_0)^{-7/3} - (V/V_0)^{-5/3}] \times \left\{1 + \frac{3}{4}(K_0' - 4)[(V/V_0)^{-2/3} - 1]\right\}, \quad (1)$$

where P is the applied pressure, V is the volume at pressure, V_0 is the room-pressure volume, K_0 is the room-pressure bulk modulus, and K_0' is the first pressure derivative of the bulk modulus at room pressure. From the thermodynamic relationship, $P=-\frac{\partial E}{\partial V}$, Eq. (1) can be integrated to obtain an expression for $E(V)$:

$$E = \frac{9K_0V_0}{2}\left\{\frac{1}{2}[(V/V_0)^{-2/3} - 1]^2\right\} \times \left[1 + (K_0' - 4)\left\{\frac{1}{2}[(V/V_0)^{-2/3} - 1]\right\}\right] + E_0, \quad (2)$$

where E_0 is the energy at the ambient pressure volume. A second-order Birch-Murnaghan EOS is given by fixing K_0' to 4 in Eqs. (1) and (2). For both the experimental and theoretical data, HfO_2 phases were fit using the second-order Birch-Murnaghan EOS to more easily compare with previous studies (Tables II and III).

TABLE II. Experimental equations of state of the HfO_2 phases. The EOSs of all phases were obtained from a second-order Birch-Murnaghan equation of state [Eq. (1) with $K_0'=4$] to our experimental results in order to determine the isothermal bulk modulus (K_0). For comparison, we list other experimental results that include angular-dispersive x-ray diffraction (ADX), energy-dispersive x-ray diffraction (EDX) and multi-anvil (MA) techniques. 1σ uncertainties are given in parentheses.

Phase	V_0 (Å^3)	K_0 (GPa)	K_0'	Reference
MI	34.50 (0.04)	185 (23)	4 (fixed)	This work (DAC+ADX)
	30.30	284 (30)	5 (2)	DAC+EDX (Ref. 5), reported values
	30.30	325 (59)	4 (fixed)	DAC+EDX (Ref. 5), revised values[a]
	34.67	145 (22)	5 (fixed)	DAC+ADX (Ref. 17), reported values
	34.67	138 (52)	4 (fixed)	DAC+ADX (Ref. 17), revised values[a]
OI	33.12 (0.13)	266 (28)	4 (fixed)	This work (DAC+ADX)
	28.93	281 (10)	4.2 (0.9)	DAC+EDX (Ref. 5), reported values
	28.93	283 (11)	4 (fixed)	DAC+EDX (Ref. 5), revised values[a]
	33.11	210 (32)	5 (fixed)	DAC+ADX (Ref. 17), reported values
	33.11	234 (37)	4 (fixed)	DAC+ADX (Ref. 17), revised values[a]
	33.17	220 (10)	4 (fixed)	MA+EDX (Ref. 4)
OII	29.74 (0.11)	331 (17)	4 (fixed)	This work (DAC+ADX)
	26.54	340 (10)	2.6 (0.3)	DAC+EDX (Ref. 5), reported values
	26.54	304 (44)	4 (fixed)	DAC+EDX (Ref. 5), revised values[a]
	29.65	312 (10)	4 (fixed)	MA+EDX (Ref. 4)

[a]We have refit the data to the second-order BM EOS to better compare results across studies.

TABLE III. Equations of state of the HfO_2 phases as obtained from GGA calculations. Our calculations were fit to a second-order Birch-Murnaghan equation of state [Eq. (2) with $K_0'=4$] to find V_0 and K_0. For comparison, we list other theoretical results. 1σ uncertainties are given in parentheses.

Phase	V_0 (Å^3)	K_0 (GPa)	K_0'	Reference
MI	35.04 (0.04)	168 (7)	4 (fixed)	GGA, this work
	34.81	152	4 (fixed)	GGA (Ref. 19)
	36.39	192	4 (fixed)	GGA (Ref. 8)
OI	33.58 (0.01)	218 (2)	4 (fixed)	GGA, this work
	33.53	197	4 (fixed)	GGA (Ref. 19)
	35.04	221	4 (fixed)	GGA (Ref. 8)
OII	30.12 (0.05)	260 (4)	4 (fixed)	GGA, this work
	31.86	251	4 (fixed)	GGA (Ref. 19)
	29.75	259	4 (fixed)	GGA (Ref. 8)

III. THEORETICAL METHODS

To study the phase relations and the EOSs of the polymorphs of HfO_2, our experiments were augmented with static *first-principles* computations performed within the framework of DFT.[41] Interactions between the atoms were treated within the projector-augmented wave (PAW) formalism,[42,43] core radii of 2.600 bohr (valence configuration: $5p^6 6s^2 5d^2$) and 1.520 bohr (valence configuration: $2s^2 2p^4$) for hafnium and oxygen, respectively. Following previous studies on HfO_2 (Refs. 8 and 19), the electronic exchange and correlation effects were treated within the generalized gradient approximation (GGA).[44] The calculations were performed using the VASP software package[45–48] with an energy cutoff of 600 eV and Γ-centered k-point meshes.[49] Total energies were converged to better than ~1 meV/atom and pressures converged to within 0.3 GPa. In our calculations, we have used the following k-point meshes for the HfO_2 phases: $4\times4\times4$ for MI, $2\times4\times4$ for OI, and $4\times8\times4$ for OII. We performed static calculations to determine the electronic ground state for each phase. Scalar relativistic effects are taken into account in the PAW potentials.[42,50] During the geometry optimizations, all internal degrees of freedom and lattice parameters were optimized simultaneously at fixed volume. The ground-state energy for each phase was determined for 6–10 volumes, which encompass the experimental pressure range for each phase. All investigated HfO_2 phases remain insulators throughout their stability ranges. The EOS parameters were obtained from the variation in the total energy with volume and fit to a second-order Birch-Murnaghan EOS (Ref. 40) [Eq. (2) with $K_0'=4$] (Table III). The pressures as derived from the second- and third-order EV EOS for OII-HfO_2 agree to within ~1% at the highest pressures of this study.

The elastic constants were calculated by applying small positive and negative strains of magnitude 1% to the relaxed equilibrium lattice. Four and six strains were used for the orthorhombic and monoclinic phases, respectively. The configuration was rerelaxed in the (fixed) strained unit cell to account for the coupling between lattice vibrations and strain. The elastic constants were obtained from linear stress/strain relationship. We calculated nine elastic constants for the orthorhombic phases (OI and OII) and 13 elastic constants for the monoclinic phase (MI). Aggregate moduli were calculated using the Voigt-Reuss-Hill (VRH) averaging scheme.[51] The mechanical hardness of each HfO_2 phase was estimated using a recently proposed scaling law that relates bond topology, electronic structure, and the mechanical hardness in covalent and ionic materials.[32]

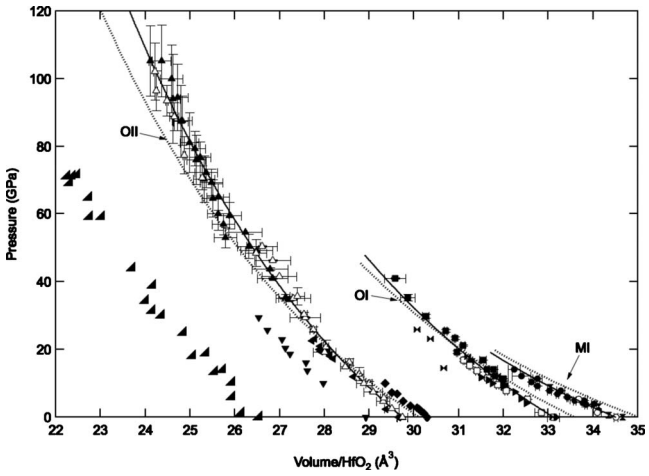

FIG. 2. Pressure versus volume of one HfO_2 formula unit as determined by experiment. MI (circles), OI (squares), and OII (triangles) volumes are shown under compression (solid symbols) and on decompression (open symbols). The solid curves indicate our experimental EOS, and the dotted curves show the predicted EOS from GGA calculations. MI: our data are close to our GGA calculations; for comparison, we list other experimental work (vertical bowties for Ref. 17 and diamonds for Ref. 5). OI: our GGA calculations go through most of our data, especially at pressures greater than 10 GPa; for comparison, we list other experimental work (horizontal bowties for Ref. 17, right-handed triangles for Ref. 4 and inverted triangles for Ref. 5). OII: our observed OII data up to ~105 GPa are in good agreement with our GGA calculations especially at pressures lower than 50 GPa; for comparison, we list other experimental work (left-handed triangles for Ref. 4 and right-angled triangles for Ref. 5).

IV. RESULTS AND DISCUSSION

A. Diamond-anvil cell experiments: Phase stability and equation of state

For all XRD patterns, all reflections are identified by NaCl, Re, or one (or more) of the three HfO_2 polymorphs MI, OI, and OII (Fig. 1). Each HfO_2 phase is described below.

1. Monoclinic MI

We observe that the room-temperature stability range of MI extends from ambient pressure to 11–14 GPa on compression (runs 1 and 2; Table I; Figs. 1 and 2), consistent with previous work.[5,17] Upon decompression from 19 GPa,

MI reappears at ~5 GPa up to ambient pressure, where MI is observed in the quenched XRD pattern along with OI (run 1; Table I). In one of the heated experiments, where the sample is heated at ~35 GPa (run 5; Table I), we also observe MI in the quenched XRD pattern in addition to the OII phase (discussed below). This is unique to run 5 as MI was not observed in any other decompression patterns heated at high pressures before quenched to room pressure.

Previous measurements of the EOS of MI show a large discrepancy in bulk modulus values that ranges from 145 (±22) GPa [K_0'=5 (fixed)] (Ref. 17) to 284 (±30) GPa [K_0'=5 (±2)] (Ref. 5) (Table II). Using a second-order Birch-Murnaghan EOS (K_0'=4), we have determined the EOS of MI by fitting all points on compression and decompression up to ~14 GPa and found K_0=185 (±23) GPa (Table II). In order to eliminate correlation between K_0 and K_0' and to compare BM-EOS values more directly with our data, we reanalyze EOSs from previous work for K_0'=4 and obtain K_0=138 (±52) GPa and 325 (±59) GPa for Refs. 17 and 5, respectively (Table II); yielding an even larger variation in K_0 values. Our K_0 of MI, within the given uncertainties, is in good agreement with the estimated value from bulk modulus-volume systematics of ~200 GPa (Ref. 22) as well as with our DFT computations (see Sec. IV B). Our MI-EOS includes more measurements of the MI phase (17 data points; Fig. 2) than previous experimental studies that are based on a smaller number of measurements (four data points for Ref. 17 and 11 points for Ref. 5).

2. Orthorhombic OI

In the unheated experiments [runs 1, 2, and 5 (before heating); Table I], prominent diffraction from OI begins at 9–11 GPa and remains present up to ~41 GPa [Figs. 1(b)–1(d)]. This is consistent with previous experiments in which OI is observed to 32 GPa at room temperature.[5] Upon decompression from 19 GPa (run 1; Table I), OI continues to be stable until 0 GPa and observed in the quenched XRD pattern along with MI phase. However, in run 4 (Table I), after heating the sample at ~20 GPa, a coexistence of OI and OII is observed until ~27 GPa. This is in agreement with previous observations of a negative Clapeyron slope of the OI→OII phase transition.[4,5,16,17]

It is important to note that we observe the first appearance of OI XRD reflections as low as 4–6 GPa (Refs. 5, 11, 14, 16, and 18) (runs 1 and 2; Table I) but OI becomes prominent only at pressures higher than 9 GPa [Fig. 1(b)].[5,16,17] Therefore, the MI→OI transition is sluggish at room temperature, which is also evidenced by the persistent appearance of the strongest reflection of MI up to ~30 GPa [Fig. 1(c)] in addition to the comparable x-ray reflection strength of MI and OI between 9 and 14 GPa (run 1; Table I). This sluggish behavior is consistent with similar transition-metal dioxide ZrO_2.[52]

In determining the EOS of OI, we use ~3x the amount of measurements (24 data points up to 41 GPa; Fig. 2) than previous experiments (six data points for Ref. 17, nine points for Ref. 5, and eight points for Ref. 4), yielding an EOS that is comparable to previous studies[4,5,17] (Table II). Using a second-order Birch-Murnaghan EOS, we find K_0=266 (±28) GPa (Table II). Our measured EOS of OI is comparable to that obtained from our DFT computations within the given uncertainties (see Sec IV B). Finally, we should point out that the data of all HfO_2 phases in Ref. 5 are shifted to smaller volumes than present and previous studies[4,17] and may suggest a clerical error in Ref. 5 (Fig. 2).

3. Orthorhombic OII

In previous high-pressure XRD experiments performed to investigate the stability of the OII phase, the maximum pressures achieved were 71 GPa (room-temperature study)[5,16] and 24 GPa (high-temperature study).[4,16] In this study, we have tested the stability and determined the EOS of this phase up to a pressure of ~105 GPa before and after laser heating to ~1800 (±200) K and find OII to be stable under these conditions.

For unheated experiments (runs 2 and 3; Table I) and for run 6 (before heating), the stability range of OII at room temperature begins at ~35 GPa (Ref. 5) and extends to the maximum pressure achieved of ~105 GPa upon compression. Upon decompression, OII is observed as the only stable phase up to zero pressure.

To test the high-pressure/temperature phase stability of OII, we have annealed our samples at various pressures to ~1800 (±200) K (runs 4–6; Table I). In run 4, after heating the sample at ~20 GPa, OII is observed above 20 GPa on compression, although a coexistence of OI and OII is observed up to 27 GPa indicating possible incomplete heating of the sample to overcome the negative Clapeyron slope of this transition. In run 4, like in runs 2 and 3, OII is observed as the only recovered phase at ambient conditions. In run 5, the sample is heated at 35 GPa, and a complete transformation from OI to OII is observed, and remains stable upon decompression from this pressure to room pressure. For run 5, in addition to OII, MI is observed in the quenched pattern. In run 6 (Table I), during cold compression, OII is the only observed stable phase from ~51 to 105 GPa, (Fig. 2). After heating at this pressure (105 GPa), we do not observe any evidence of a new phase. However, heating releases the deviatoric stresses and, as a result, much sharper XRD peaks are observed after heating [Figs. 1(f) and 1(g)].

The measured EOS of OII compares well with previous measurements[4] (Table II, Fig. 2) while for Ref. 5 the given data points are shifted to much smaller volumes than observed in our and other previous work.[4] Using a second-order Birch-Murnaghan EOS, we have measured our EOS of OII taken during compression and decompression that covers a pressure range from 0 to 105 GPa (Fig. 2). Our measured K_0=331 (±17) GPa when K_0' is fixed to 4; or using a third-order Birch-Murnaghan EOS, we obtain K_0=328 (±8) GPa and K_0'=4.03. The wide pressure range of our experiments yields a good fit for K_0' and shows that a second-order Birch-Murnaghan EOS is a reasonable assumption.

The experimentally observed volume change across OI→OII transition is ~8.6% (Fig. 2) in good agreement with previous measurements on HfO_2 (Refs. 4, 5, and 16) and similar transition-metal dioxides [e.g., ZrO_2 (Refs. 5 and 52) and TiO_2 (Ref. 53)]. In addition to this large volume collapse, at ambient conditions, OII is denser than MI and OI by

13.8% and 10.2%, respectively (Table II). This indicates that OII is a high-density phase and also observed to be the most stable phase at the highest pressure of our study of 105 GPa consistent with previous experiments which extended over a smaller pressure range.[4,5,12,16]

B. First-principles calculations: Phase stability and equation of state

To compare our computed HfO_2 EOSs with our experimental measurements, we plot volume versus pressure (Fig. 2) and find reasonable agreement. However, in detail, the EOS parameters are different (Tables II and III). These differences arise at least partly from the well-known correlation of V_0 and K_0: as V_0 decreases, K_0 increases. Also, it is well known that GGA generally overestimates volumes and, as a result, underestimates K_0;[53–55] therefore, differences are not unexpected. Combining the effect of the correlation between V_0 and K_0 with our uncertainties in K_0 values, our measured and calculated EOSs are consistent with each other (Tables II and III). Furthermore, our calculated EOSs are comparable to previous calculations using GGA (Refs. 8 and 19) (Table III). Consequently, for the MI phase, our and previous computations[8,19] support an intermediate K_0 value in agreement with our measured value [185 ($\pm$23) GPa] and those estimated from bulk modulus-volume systematics ($\sim$200 GPa).[22]

The predicted transition pressure from MI to OI occurs at 9.1 GPa, in good agreement with our and previous experimental observations[5,17] (Table I) and previous computations.[19] For the OI$\rightarrow$OII transition, our calculations predict a transition pressure of 16.8 GPa; which is lower than our experimental observations at room temperatures, although consistent our heated experiments (run 4; Table I) and previous high *P-T* experiments,[4] and in good agreement with previous calculations.[19]

Finally, our calculated volume change across the OI $\rightarrow$OII transition is large and has a value of 9.5% that compares well with our experimental observations of 8.6% as well as with previous experimental[4,5,16] and theoretical[8,19] work performed on HfO_2 and similar dioxides.[19,52,53]

C. Mechanical strength of HfO_2 phases

The OII phase has been speculated to be much harder than the low-pressure phases MI and OI due to its comparatively high density and large bulk modulus.[3–8] In this section, we analyze this assumption. We have performed *first-principles* computations to estimate the hardness and the elastic constants of the experimentally observed room-temperature HfO_2 phases.

1. Hardness calculations

The experimentally available hardness values of room-temperature HfO_2 phases are measurements for MI and OII phases. For MI, a hardness value of 9.9 GPa (Ref. 56) has been measured for pure HfO_2. For OII-HfO_2, a hardness between 6 and 13 GPa (Ref. 10) has been reported for samples quenched from 20 GPa and 800 °C. The significant scatter was attributed to poor sintering of the sample.

Using the Simunek and Vackar scaling model,[32] we estimate the mechanical hardness of our experimentally observed ambient temperature HfO_2 polymorphs. In this model, the hardness increases with decreasing average atomic volume (as expected), increasing average number of bonds per atom, decreasing coordination number, and decreasing average bond length.[32,57] In addition to crystal chemistry, the hardness depends also on the characteristic length scale (R_i) of the charge-density distribution about each atom. These radii are determined iteratively such that the spatially integrated charge density within a spherical volume of radius R_i agrees with the number of valence electrons for each atomic species.[32] Using this method, we obtain $R(\mathrm{Hf})=1.78$ Å and $R(\mathrm{O})=1.07$ Å using GGA. We note that the implied ratio ($e_i=Z_i/R_i$) for oxygen, $e(\mathrm{O})=6/1.07=5.608$, is very similar to the independently derived value for oxygen in ZrO_2, $e(\mathrm{O})=5.556$,[52] and in fluorite type TiO_2, $e(\mathrm{O})=5.964$.[58] In agreement with Refs. 32 and 57, we find that the radii do not depend strongly on the phase; differences in radii between MI, OI, and OII are less than 1%. The calculated hardness value of the MI phase is 11.4 GPa, which compares well with the available experimental value of 9.9 GPa (Ref. 56) (Table IV). Our predicted value is also consistent with the estimated value from another hardness model[60] which gives a hardness value of 9.8 GPa. For the higher pressure phases OI and OII, we predict hardness values of 11.9 GPa and 9.8 GPa, respectively. Thus, we predict that the hardness depends only weakly on phase and that the order of the estimated hardness values differs from the observed bulk modulus sequence in HfO_2, i.e., $H(\mathrm{OII})<H(\mathrm{MI})<H(\mathrm{OI})$ (Table IV). Furthermore, the predicted hardness values and trend for HfO_2 phases are consistent with that of isomorphic ZrO_2.[52] We would like to note that within this scaling model,[32] the estimated hardness trend depends on the atomic volume and the bond-length distribution (bond distance, number of bonds, and the coordination number). Thus, hardness increases with decreasing volume and decreasing bond length (for fixed coordination number). However, the volume decrease in OII is counteracted by coordination number increase (from seven in OI to nine in OII) that is also associated with an increase in the bond length. On the other hand, for MI and OI, Hf atom is sevenfold coordinated, and their specific volumes (Tables II and III), and average bond lengths are similar, and, as a result, their hardness values are very similar (Table IV). The large specific volume decrease across OI$\rightarrow$OII transition of $\sim$9% is compensated by the coordination increase in Hf atom from seven to nine which is associated with an average bond length increase of $\sim$6%. This increase is mainly due to the lengthening of the shortest Hf-O bond and the two longest nearest-neighbor distances. The combined effect is that the hardness of OII is slightly lower than that of the OI phase, opposite to what would be expected if the specific volume alone would dominate hardness. Thus, the estimated hardness in HfO_2 phases depends on the details of crystal chemistry and nearest-neighbor bond-length distribution. However, our estimated hardness of the OII phase as nonsuperhard material is independent of the detailed treatment of the crystal chemistry.

Using the experimentally observed crystal structures for MI, OI, and OII, we find that the predicted hardness values

TABLE IV. Calculated hardness of HfO_2 using the Simunek and Vackar covalent model formalism. CN is the coordination number of Hf atoms. Our shear and bulk moduli are also given from Tables II, III, and V to compare their trends with hardness. For comparison, we list available experimental measurements for MI, OI, and OII, along with values predicted (in italics) by the Simunek formalism (Ref. 57) for measured bond distances. Unless otherwise noted, listed values are from this study. 1σ uncertainties are given in parentheses. For values not available, NA is recorded.

		K_0 (GPa)		G (GPa)		H (GPa)	
Phase	CN	Theory	Experiment	Theory	Experiment	Theory	Experiment
MI	7	168 (7)	185 (23)	98.7	109[a]	11.4 *12.9*[b]	9.9[c]
OI	7	218 (2)	266 (28)	115.5	NA	11.9 *13.4*[b]	NA
OII	9	260 (4)	331 (17)	93.4	NA	9.8 *11.1*[b]	6–13[d]

[a]Reference 59.
[b]Hardness values estimated using scaling relations discussed in Ref. 57 by using experimental bond distances given in Refs. 61, 15, and 12 for MI, OI, and OII bond distances, respectively, in addition to our measured V_0.
[c]Reference 56.
[d]Reference 10.

based on our computed and experimental equilibrium structures [MI,[61] OI,[15] and OII (Ref. 12)] agree to within 1.5 GPa (Table IV). Thus, the use of the optimized GGA equilibrium structures does not significantly bias the hardness estimates to low values at least in the case of hafnia.

2. Elastic constants and shear moduli calculations

Previous studies suggest a correlation between shear modulus and hardness with higher shear moduli correspond to a higher hardnesses.[27,28] If this is satisfied, then one can expect that both shear modulus and hardness should show the same trend for the same material. We test this possibility with the calculation of the elastic constants and corresponding shear modulus for each HfO_2 phase.

Due to the difficulty in measuring the shear moduli of materials, G has only been measured for MI.[59] Currently, the only available elastic constants for room-temperature HfO_2 polymorphs are predictions for the highest-pressure phase OII (Table V).[29,30] To fill this gap and to test shear modulus-hardness systematics, we used *first-principles* computations to calculate the complete elastic constant tensor for the three experimentally observed HfO_2 phases. Using the calculated elastic constants for the MI, OI, and OII phases (Table V), we obtain the VRH average of the shear modulus: $G(\mathrm{OII};93.4\ \mathrm{GPa}) < G(\mathrm{MI};98.7\ \mathrm{GPa}) < G(\mathrm{OI};115.5\ \mathrm{GPa})$ consistent with the order of the predicted hardness values (Table IV). On the other hand, both our measured or calculated bulk moduli (Table IV) increase with each higher pressure phase, consistent with previous suggestions that the shear modulus may better correlate with hardness values than the bulk modulus.[27,28]

We should also note that the calculated VRH bulk modulus of OII as obtained from the elastic constants calculations (Table V) is smaller than that obtained from the BM-EOS fits (Table III) by ~13%, close to the K_0 value of OI (Table V). Additionally, K_0(OI) from Table V is in good agreement with the corresponding value given in Table III. However, when

TABLE V. Calculated elastic constants of HfO_2 phases and corresponding shear moduli. For comparison, we list other theoretical results.

			OII		
Physical property (GPa)	MI (this work)	OI (this work)	This work	GGA[a]	Empirical model potential[b]
C_{11}	340.9	374.7	458.4	502	477
C_{22}	392.8	436	326	261	415
C_{33}	288.2	391.3	365.9	597	446
C_{44}	86.9	97.8	51	78	31
C_{55}	93.5	97.1	81.5	90	117
C_{66}	131.5	128.3	133.6	111	132
C_{12}	164.4	160.3	154.5	122	172
C_{13}	107	128.6	184.2	159	202
C_{15}	41.9				
C_{23}	158.6	130	121.4	244	151
C_{25}	−8.4				
C_{35}	−0.4				
C_{46}	−9.9				
G	98.7	115.5	93.4	103	94.6
K_0	203.9	225.9	225.5	246	264

[a]Reference 29.
[b]Reference 30.

we fit *PV*-GGA data of OI and OII using the third-order BM EOS, we obtain $K_0=222$ GPa with $K_0'=3.29$ for OI and $K_0=229$ GPa with $K_0'=5.07$ for the OII phase. Thus, the observed differences in the OII phase can be explained by the type of fit (i.e., second- or third-order BM EOS) or, in other words, are related to the value of K_0'.

This analysis shows that it is unlikely that any of the currently known HfO_2 polymorphs qualify as superhard. In particular, experimental observations of the hardness of OII-HfO_2 that were regarded as low due to poor sintering[10] are likely a reflection of the low intrinsic hardness of this phase rather than related to the microstructure in the sample.

It is important to point out that the hardness-phase relationship observed for HfO_2 system is not universal; for this system, we notice a weak dependence of hardness on phase. To contrast, the graphite→diamond [62,63] and quartz →stishovite [64–68] phase transitions yield a dramatic increase in hardness. Thus, the hardness-phase relationship depends on the detailed changes in crystal chemistry (e.g., coordination number, specific volume, bond nature, and crystal structure) across a phase transition. However, in HfO_2 and the given counterexamples, the correlation between shear modulus and hardness is still satisfied.[62–68]

V. CONCLUSIONS

We have used both DAC experiments using high-resolution synchrotron-based XRD and DFT-based *first-principles* computations to study the high-pressure behavior and mechanical strength of hafnia. The stability range of each phase was studied to better understand the phase diagram of this dioxide and the high-pressure synthesis route of mechanically stronger materials. In this study, we provide revised experimental EOSs for the low-pressure phases MI and OI, which are comparable to our DFT EOSs. Furthermore, our experiments show that the OII phase is stable up to at least 105 GPa with no evidence of a new phase up to this pressure, and this is supported by our *first-principles* calculations. Our measured EOS of OII up to the maximum pressure achieved is in good agreement with previous studies. Additionally, the OII-HfO_2 phase is observed to be much denser than the low-pressure phases. Across the OI→OII transition, the volume reduces by ~9% and compares well with the volume collapse in other isostructural dioxides.[5,52,53] As the high-density OII-HfO_2 phase is quenchable to ambient conditions, we have studied its mechanical strength in comparison to the other low-pressure phases. In addition to OII, we have calculated the elastic constants of MI and OI-HfO_2 phases to better understand the correlations between the shear/bulk moduli and hardness. We explore the hardness of the OII-HfO_2 phase using scaling relations and find, in contrast to what has been suggested,[3–8] that the hardness of this phase is predicted to be comparable to MI and OI phases and much lower than 40 GPa, a prerequisite for a material to qualify as superhard. Interestingly, the low-pressure phases (MI and OI) show a slightly greater mechanical strength than OII, although the differences are within mutual uncertainties. The hardness values are too low for any of the observed hafnia phases to qualify as superhard. Thus, the low hardness is an intrinsic property of hafnia and similar oxides as opposed to previous observations that attributed the low hardness of hafnia to poorly sintered samples.[10] The low mechanical strength of the OII phase is mainly the result of an increased shortest Hf-O bond length and coordination number as compared to MI and OI phases that compensates the opposing effects of the low specific volume. Finally, we successfully combine experiment and theory to explore the relationship between mechanical strength and phase in the case of HfO_2. Given these results, phases synthesized at high pressure do not universally result in improved mechanical characteristics and the relationship between hardness and incompressibility is not necessarily correlated.

ACKNOWLEDGMENTS

Portions of this work were performed at HPCAT (XRD, laser heating), Advanced Photon Source (APS), Argonne National Laboratory; and at B2 (XRD), Cornell High Energy Synchrotron Source (CHESS), Cornell University. HPCAT is supported by DOE-BES, DOE-NNSA, NSF, and the W.M. Keck Foundation. APS and CHESS are supported by DOE. Y.A-K. and K.K.M.L. acknowledge support from CDAC. We also thank the beamline scientists at HPCAT and B2 beamlines, Yue Meng and Zhongwu Wang, for their cooperation and help.

[1] K. Mergia, V. Liedtke, T. Speliotis, G. Apostolopoulos, and S. Messoloras, Adv. Mater. Res. **59**, 87 (2009).
[2] V. Fiorentini and G. Gulleri, Phys. Rev. Lett. **89**, 266101 (2002).
[3] J. E. Lowther, J. K. Dewhurst, J. M. Leger, and J. Haines, Phys. Rev. B **60**, 14485 (1999).
[4] O. Ohtaka, H. Fukui, T. Kunisada, T. Fujisawa, K. Funakoshi, W. Utsumi, T. Irifune, K. Kuroda, and T. Kikegawa, J. Am. Ceram. Soc. **84**, 1369 (2001).
[5] S. Desgreniers and K. Lagarec, Phys. Rev. B **59**, 8467 (1999).
[6] J. K. Dewhurst and J. E. Lowther, Phys. Rev. B **64**, 014104 (2001).
[7] J. E. Lowther, MRS Bull. **28**, 189 (2003).
[8] J. Kang, E.-C. Lee, and K. J. Chang, Phys. Rev. B **68**, 054106 (2003).
[9] J. M. Léger, J. Haines, and B. Blanzat, J. Mater. Sci. Lett. **13**, 1688 (1994).
[10] J. Haines, J. M. Leger, M. Schmidt, J. P. Petitet, A. S. Pereira, and J. A. H. da Jornada, in *Proceeding of the XXXIV EHPRG Conference*, edited by K. Heremans (Leuven University Press, Leuven, Belgium, 1997), p. 13.
[11] D. M. Adams, S. Leonard, D. R. Russell, and R. J. Cernik, J. Phys. Chem. Solids **52**, 1181 (1991).
[12] J. Haines, J. M. Leger, S. Hull, J. P. Petitet, A. S. Pereira, C. A. Perottoni, and J. A. H. da Jornada, J. Am. Ceram. Soc. **80**, 1910

(1997).
[13] A. Jayaraman, S. Y. Wang, S. K. Sharma, and L. C. Ming, Phys. Rev. B **48**, 9205 (1993).
[14] O. Ohtaka, T. Yamanaka, S. Kume, and F. Izumi,J. Ceram. Soc. Jpn. **99**, 826 (1991).
[15] O. Ohtaka, T. Yamanaka, S. Kume, N. Hara, and H. Asano, J. Am. Ceram. Soc. **78**, 233 (1995).
[16] J. Tang, M. Kai, Y. Kobayashi, S. Endo, O. Shimomura, T. Kikegawa, and T. Ashida, in *Properties of Earth and Planetary Materials at High Pressure and Temperature*, edited by M. H. Manghnani and T. Yagi (American Geophysical Union, Washington, DC, 1998).
[17] J. M. Leger, A. Atouf, P. E. Tomaszewski, and A. S. Pereira, Phys. Rev. B **48**, 93 (1993).
[18] H. Arashi, J. Am. Ceram. Soc. **75**, 844 (1992).
[19] J. E. Jaffe, R. A. Bachorz, and M. Gutowski, Phys. Rev. B **72**, 144107 (2005).
[20] J. Wang, H. P. Li, and R. Stevens, J. Mater. Sci. **27**, 5397 (1992).
[21] P. E. Quintard, P. Barberis, A. P. Mirgorodsky, and T. Merle-Mejean, J. Am. Ceram. Soc. **85**, 1745 (2002).
[22] O. L. Anderson, *The Nature of the Solid Earth* (McGraw-Hill, New York, 1972).
[23] J. M. Leger and J. Haines, Endeavour **21**, 121 (1997).
[24] J. Z. Hu, H. K. Mao, J. F. Shu, Q. Z. Guo, and H. Z. Liu, J. Phys.: Condens. Matter **18**, S1091 (2006).
[25] J. Z. Jiang, H. Lindelov, L. Gerward, K. Ståhl, J. M. Recio, P. Mori-Sanchez, S. Carlson, M. Mezouar, E. Dooryhee, A. Fitch, and D. J. Frost, Phys. Rev. B **65**, 161202(R) (2002).
[26] A. Zerr, G. Miehe, G. Serghiou, M. Schwarz, E. Kroke, R. Riedel, H. FueB, P. Kroll, and R. Boehler, Nature (London) **400**, 340 (1999).
[27] D. M. Teter, MRS Bull. **23**, 22 (1998).
[28] J. Haines, J. M. Leger, and G. Bocquillon, Annu. Rev. Mater. Res. **31**, 1 (2001).
[29] M. A. Caravaca, J. C. Mino, V. J. Perez, R. A. Casali, and C. A. Ponce, J. Phys.: Condens. Matter **21**, 015501 (2009).
[30] A. P. Mirgorodsky and P. E. Quintard, J. Am. Ceram. Soc. **82**, 3121 (1999).
[31] C. A. Ponce, R. A. Casali, and M. A. Caravaca, J. Phys.: Condens. Matter **20**, 045213 (2008).
[32] A. Šimůnek and J. Vackář, Phys. Rev. Lett. **96**, 085501 (2006).
[33] I. Fujishiro, G. J. Piermarini, S. Block, and R. G. Munro, in *Proceedings of the 8th AIRAPT Conference*, edited by C. M. Backman, T. Johannisson, and L. Tenger (Arkitektkopia, Uppsala, Sweden, 1982), p. 608.
[34] Y. Sato-Sorensen, J. Geophys. Res. **88**, 3543 (1983).
[35] D. L. Heinz and R. Jeanloz, Phys. Rev. B **30**, 6045 (1984).
[36] H. K. Mao, J. Xu, and P. M. Bell, J. Geophys. Res. **91**, 4673 (1986).
[37] Y. Meng, G. Shen, and H. K. Mao, J. Phys.: Condens. Matter **18**, S1097 (2006).
[38] A. P. Jephcoat and S. P. Besedin, Philos. Trans. R. Soc. London, Ser. A **354**, 1333 (1996).
[39] A. P. Hammersley, S. O. Svensson, M. Hanfland, A. N. Fitch, and D. Hausermann, High Press. Res. **14**, 235 (1996).
[40] F. Birch, J. Geophys. Res. **57**, 227 (1952).
[41] P. Hohenberg and W. Kohn, Phys. Rev. **136**, B864 (1964).
[42] G. Kresse and D. Joubert, Phys. Rev. B **59**, 1758 (1999).
[43] P. E. Blöchl, Phys. Rev. B **50**, 17953 (1994).
[44] J. P. Perdew, K. Burke, and M. Ernzerhof, Phys. Rev. Lett. **77**, 3865 (1996).
[45] G. Kresse and J. Furthmuller, Comput. Mater. Sci. **6**, 15 (1996).
[46] G. Kresse and J. Furthmuller, Phys. Rev. B **54**, 11169 (1996).
[47] G. Kresse and J. Hafner, Phys. Rev. B **48**, 13115 (1993).
[48] G. Kresse and J. Hafner, J. Phys.: Condens. Matter **6**, 8245 (1994).
[49] H. J. Monkhorst and J. D. Pack, Phys. Rev. B **13**, 5188 (1976).
[50] L.-L. Wang and D. D. Johnson, J. Phys. Chem. B **109**, 23113 (2005).
[51] R. Hill, Proc. Phys. Soc., Sect. A **65**, 349 (1952).
[52] Y. Al-Khatatbeh, K. K. M. Lee, and B. Kiefer, Phys. Rev. B **81**, 214102 (2010).
[53] Y. Al-Khatatbeh, K. K. M. Lee, and B. Kiefer, Phys. Rev. B **79**, 134114 (2009).
[54] R. E. Cohen, I. I. Mazin, and D. G. Isaak, Science **275**, 654 (1997).
[55] L. Stixrude, R. E. Cohen, and D. J. Singh, Phys. Rev. B **50**, 6442 (1994).
[56] M. Okutomi, K. Kasamatsu, S. Tsukamoto, S. Shiratori, and F. Uchiyama, Appl. Phys. Lett. **44**, 1132 (1984).
[57] A. Šimůnek, Phys. Rev. B **75**, 172108 (2007).
[58] Y. Liang, B. Zhang, and J. Zhao, Phys. Rev. B **77**, 094126 (2008).
[59] S. L. Dole, O. Hunter, and C. J. Wooge, J. Am. Ceram. Soc. **60**, 488 (1977).
[60] F. Gao, J. He, E. Wu, S. Liu, D. Yu, D. Li, S. Zhang, and Y. Tian, Phys. Rev. Lett. **91**, 015502 (2003).
[61] R. Ruh and P. W. R. Corfield, J. Am. Ceram. Soc. **53**, 126 (1970).
[62] J. R. Patterson, S. A. Catledge, Y. K. Vohra, J. Akella, and S. T. Weir, Phys. Rev. Lett. **85**, 5364 (2000).
[63] R. A. Andrievski, Int. J. Refract. Met. Hard Mater. **19**, 447 (2001).
[64] J. H. Westbrook and H. Conrad, *The Science of Hardness Testing and Its Research Applications* (ASM, Ohio, 1973).
[65] J. M. Léger, J. Haines, M. Schmidt, J. P. Petitet, A. S. Pereira, and J. A. H. da Jornada, Nature (London) **383**, 401 (1996).
[66] H. J. McSkimin, P. Andreatch, and R. N. Thurston, J. Appl. Phys. **36**, 1624 (1965).
[67] B. Holm and R. Ahuja, J. Chem. Phys. **111**, 2071 (1999).
[68] D. J. Weidner, J. D. Bass, A. E. Ringwood, and W. Sinclair, J. Geophys. Res. **87**, 4740 (1982).